













RESEARCH ARTICLE | SEPTEMBER 09 2024

# Toward the reproducible fabrication of conductive ferroelectric domain walls into lithium niobate bulk single crystals

Julius Ratzenberger  ; Luliia Kiseleva  ; Boris Koppitz  ; Elke Beyreuther   ; Manuel Zahn  ; Joshua Gössel  ; Peter A. Hegarty  ; Zeeshan H. Amber  ; Michael Rüsing  ; Lukas M. Eng 

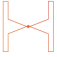
 Check for updates


*J. Appl. Phys.* 136, 104302 (2024)


<https://doi.org/10.1063/5.0219300>


  
View  
Online


  
Export  
Citation

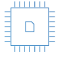
 Nanotechnology & Materials Science


 Optics & Photonics

 Impedance Analysis

 Scanning Probe Microscopy

 Sensors


 Failure Analysis & Semiconductors



## Unlock the Full Spectrum. From DC to 8.5 GHz.

Your Application. Measured.

[Find out more](#)



# Toward the reproducible fabrication of conductive ferroelectric domain walls into lithium niobate bulk single crystals

Cite as: J. Appl. Phys. **136**, 104302 (2024); doi: [10.1063/5.0219300](https://doi.org/10.1063/5.0219300)

Submitted: 16 May 2024 · Accepted: 23 August 2024 ·

Published Online: 9 September 2024



Julius Ratzenberger,<sup>1,2</sup> Iuliia Kiseleva,<sup>1</sup> Boris Koppitz,<sup>1</sup> Elke Beyreuther,<sup>1,a)</sup> Manuel Zahn,<sup>1,3</sup> Joshua Gössel,<sup>1</sup> Peter A. Hegarty,<sup>1</sup> Zeeshan H. Amber,<sup>1</sup> Michael Rüsing,<sup>4</sup> and Lukas M. Eng<sup>1,2</sup>

## AFFILIATIONS

<sup>1</sup>Institut für Angewandte Physik, Technische Universität Dresden, 01062 Dresden, Germany

<sup>2</sup>ct.qmat: Dresden-Würzburg Cluster of Excellence—EXC 2147, Technische Universität Dresden, 01062 Dresden, Germany

<sup>3</sup>Center for Electronic Correlations and Magnetism, University of Augsburg, 86159 Augsburg, Germany

<sup>4</sup>Institute for Photonic Quantum Systems, Paderborn University, 33098 Paderborn, Germany

<sup>a)</sup>Author to whom correspondence should be addressed: [elke.beyreuther@tu-dresden.de](mailto:elke.beyreuther@tu-dresden.de)

## ABSTRACT

Ferroelectric domain walls (DWs) are promising structures for assembling future nano-electronic circuit elements on a larger scale since reporting domain wall currents of up to 1 mA per single DW. One key requirement hereto is their reproducible manufacturing by gaining preparative control over domain size and domain wall conductivity (DWC). To date, most works on DWC have focused on exploring the fundamental electrical properties of individual DWs within single-shot experiments, with an emphasis on quantifying the origins of DWC. Very few reports exist when it comes to comparing the DWC properties between two separate DWs, and literally nothing exists where issues of reproducibility in DWC devices have been addressed. To fill this gap while facing the challenge of finding guidelines for achieving predictable DWC performance, we report on a procedure that allows us to reproducibly prepare single hexagonal domains of a predefined diameter into uniaxial ferroelectric lithium niobate single crystals of 200 and 300  $\mu\text{m}$  thickness, respectively. We show that the domain diameter can be controlled with an uncertainty of a few percent. As-grown DWs are then subjected to a standard procedure of current-limited high-voltage DWC enhancement, and they repetitively reach a DWC increase of six orders of magnitude. While all resulting DWs show significantly enhanced DWC values, their individual current–voltage (I–V) characteristics exhibit different shapes, which can be explained by variations in their 3D real structure reflecting local heterogeneities by defects, DW pinning, and surface-near DW inclination.

© 2024 Author(s). All article content, except where otherwise noted, is licensed under a Creative Commons Attribution-NonCommercial-NoDerivs 4.0 International (CC BY-NC-ND) license (<https://creativecommons.org/licenses/by-nc-nd/4.0/>). <https://doi.org/10.1063/5.0219300>

## I. INTRODUCTION

In recent decades, lithium niobate ( $\text{LiNbO}_3$ , LN) has become a subject of intense research and application in various fields, ranging from ferroelectric (FE) random-access memories<sup>1</sup> and rectifying junctions<sup>2–4</sup> to memristors,<sup>5,6</sup> transistors,<sup>7,8</sup> as well as a wide range of photonic and optical devices.<sup>9–11</sup> This popularity stems from LN's high Curie temperature, low optical damage, and commercial availability since usually grown by the Czochralski method.<sup>12–14</sup> With such versatility, stability, and accessibility, LN is often referred to as representing the “silicon of photonics.”<sup>15</sup>

Apart from its importance in photonics, one of the most captivating aspects of LN lies in its domain wall conductance (DWC), which can be induced purposely at the boundaries between ferroelectric (FE) domains. Domain walls (DWs) display unique electrical properties, with conductivities reaching values that are orders of magnitude larger as compared to the surrounding bulk material.<sup>16–18</sup> This characteristic makes DWs promising candidates for exploration in nanoelectronics, offering opportunities for rewritable electronics,<sup>19</sup> applications as components in neuromorphic electronics,<sup>20</sup> or to assemble faster and energy-efficient electronic components.<sup>21</sup> Their responsiveness to external stimuli,

24 September 2024, 11:46:39

such as electric fields<sup>16,22</sup> or mechanical strain fields,<sup>23</sup> opens up the door to engineering DWC-based devices, including non-volatile memories,<sup>1</sup> memristors,<sup>5,6</sup> *pn*-junctions,<sup>3,24</sup> and transistors.<sup>7,8</sup>

Despite this huge potential and bright perspective, the determination of all factors that influence the charge transport along DWs and the reproducible engineering of such charged DWs (CDWs) into advanced devices are hindered by two factors, i.e., the lack of (a) understanding the underlying physical mechanisms and (b) protocols describing the manufacturing of identical CDW objects. Concerning the first aspect, some works have recently (i) addressed the question of *which transport phenomena* are relevant for DWC,<sup>18,25,26</sup> (ii) measured typical activation energies,<sup>18</sup> and (iii) extracted charge carrier-types by different methods ranging from magneto-electric resistance<sup>27</sup> toward two-terminal AFM-tip based<sup>28,29</sup> and standard four-point probe Hall measurements.<sup>30,31</sup> However, the aspect of finding reliable CDW manufacturing routes is exactly the starting point of the present investigation.

Regarding the production of CDWs, methods that allow for the local generation of domains are required. Notably, in many experimental applications, the preferred tools hereto are AFM-tip writing and UV-assisted poling. While the first technique is preferentially selected for writing domains into thinner films, the latter allows the creation of singular domains (and walls) into macroscopically thick crystals that measure hundreds of  $\mu\text{m}$  in thickness. Such bulk single crystals are ideal model systems to study the underlying physics of DWC due to well discriminate interface-related and DW-induced transport effects.<sup>18</sup> Notably, some literature exists reporting on the method of laser-assisted CDW production in LN, which is able to significantly lower the electric field<sup>32–34</sup> as applied for local poling. Nonetheless, *systematic* investigations of the correlation between relevant process parameters and the resulting domain size and structure are missing to date. However, such a lack of reproducibility introduces uncertainties in device characteristics, impacting reliability, functionality, and performance, clearly not matching industry standards. Therefore, addressing the reproducibility challenge is vital to fully harness the potential of CDWs and to push advancements in FE-based devices.

In this article, we embark on a comprehensive investigation of more than 60 samples having CDWs engineered into 200- and 300- $\mu\text{m}$ -thick single crystals of 5 mol. % MgO-doped LiNbO<sub>3</sub> (LN), in order to develop a poling protocol and procedure that allows one to achieve reproducible fabrication of CDWs. We provide a detailed description of a home-built, automated, computer-controlled setup for domain fabrication via UV-assisted liquid-electrode poling and analyze factors influencing domain formation, in particular, their area  $A_d$ . These include the applied electric field  $E$  upon poling, the field exposure time  $t_p$ , and the substrate's chemical composition through the comparison of different LN wafers. Based on these findings, we propose a standardized protocol to facilitate reproducible domain creation. Furthermore, we explore a process, first developed by Godau *et al.*,<sup>16</sup> to *enhance* the conductivity of as-created DWs by many orders of magnitude via post-poling high-voltage (HV) treatment, delving deeper into that effect through statistical analysis of a large number of identically prepared samples. As a key result, we find that the latter process should be carried out in a *current—instead of voltage—limited* way in order to prevent irreversible domain ex- and/or implosion effects as reported earlier.<sup>22</sup>

## II. MATERIALS AND METHODS

### A. Samples

LN is commercially available as a uniaxial FE material with a large optical bandgap of  $E_{\text{gap}} = 4.0 \text{ eV}$ .<sup>35</sup> Its singular polarization axis runs parallel to the crystallographic *z*- or *c*-axis. In the following, we refer to two different polarization directions and the respective terminating surfaces as *z*- and *z*+. All samples used in this study measure typically  $5 \times 6 \text{ mm}^2$  in the *x*-*y*-direction and are cut out from three different wafers supplied by Yamaju Ceramics Co., Ltd. (Japan), all with the same nominal doping concentration of 5 mol. % MgO. In detail, these include two *z*-cut LN wafers of 200  $\mu\text{m}$  thickness each and purchased one year apart from each other (2019 and 2020). Furthermore, in 2022, we acquired a third *z*-cut LN wafer from the same company with 300  $\mu\text{m}$  thickness. Naturally, these three wafers were produced from three distinct boules in different years and, hence, allow us to study whether or not domain growth and DWC might change when comparing wafers from one and the same manufacturer. Note that we and others<sup>33</sup> had observed that wafers from different sources may show slight variations in domain growth, e.g., in a domain propagation velocity, despite nominally having the same specifications, i.e., 5 mol. % MgO-doping.

Throughout this publication, we label all samples that contain DWs as A–B–C, with A = 1, 2, 3 declaring the three wafers purchased in 2019, 2020, and 2022, respectively, B = 200 or 300 being the wafer thickness (in  $\mu\text{m}$ ), and C being the consecutive sample serial number during our investigations. As an example, “sample 1-200-3” refers to the third sample from wafer 1, with a thickness of 200  $\mu\text{m}$ . Furthermore, the samples are grouped within the so-called *batches*, containing six to eight specimens per batch. Each batch allows for comparison with respect to the concrete influence of one or more process parameters on the domain area and/or the final current–voltage (*I*-*V*) characteristics. All samples host one single hexagonal FE domain and its respective DWs, the latter being prepared under varying conditions as specified in Table I (quick guide) and Sec. A of the [supplementary material](#) (a full-length table containing all 63 single samples of this work) and explained in the following paragraphs in detail.

### B. Growing hexagonally shaped domains by UV-assisted liquid-electrode poling

We constructed a UV-light-assisted poling setup to grow our domain structures, as depicted in Fig. 1(a). During a typical domain poling procedure, the 325-nm HeCd laser (Kimmon Koha IK3301R-G) is focused onto the *z*+ crystal surface using an apochromatic lens with NA = 0.3 to a spot size of around 4.5  $\mu\text{m}$  in diameter. At this wavelength, the crystals exhibit a low absorption coefficient<sup>36</sup> of  $\alpha = 0.5 \text{ mm}^{-1}$ , resulting in a  $1/e$ -penetration depth of 2 mm, which, hence, implies full penetration across all samples. The incident power was kept constant at  $2.8 \times 10^{-5} \text{ W/cm}^2$  for all experiments. That value was chosen as the favorable power value after a preliminary investigation to evaluate the impact of the applied laser beam power on the resulting domain area  $A_d$  by using sample batch 1.4 (see Sec. H of the [supplementary material](#) for details).

24 September 2024, 11:46:39

**TABLE I.** Short overview of the sample batches of this study, the respective domain fabrication (“poling”) parameters, and—if applicable—parameters of the domain wall conductivity (DWC) enhancement process. The table also contains information on whether I–V curves after domain growth and after “enhancement” were captured or not (symbolized by “+” or “–,” respectively), as well as the specific type of investigation(s), for which every sample batch had been assigned. A more detailed list containing every individual sample can be found in Sec. A of the [supplementary material](#). Note that batches 1.4 and 1.5, which were used only within preliminary experiments exclusively dedicated to finding the most reasonable laser power and NaCl concentration for the liquid electrodes, are omitted here.

| Batch | Labels          | Poling parameters  | DWC-enhancement parameters                                | I–V-data | Purpose(s) of investigation   |
|-------|-----------------|--|---|----------|---|
| 1.1   | 1-200-1,...,8   | $E = 4.0 \text{ kV/mm}$ ;<br>$t_p = 30 \text{ s}$                | –   | –        | Reproducibility of $A_d$  |
| 1.2   | 1-200-9,...,15  | $E = 4.0 \text{ kV/mm}$ ;<br>$t_p = 10\text{--}180 \text{ s}^a$  | $v = 4 \text{ V/s}$ ;<br>$V_{\text{max}} = 500 \text{ V}$ | ++       | $A_d = f(t_p) @ E = 4.0 \text{ kV/mm}$ ;<br>reproducibility of final I–V curves |
| 1.3   | 1-200-16,...,22 | $E = 4.5 \text{ kV/mm}$ ;<br>$t_p = 10\text{--}180 \text{ s}^a$  | $v = 4 \text{ V/s}$ ;<br>$V_{\text{max}} = 500 \text{ V}$ | ++       | $A_d = f(t_p) @ E = 4.5 \text{ kV/mm}$ ;<br>reproducibility of final I–V curves |
| 2.1   | 2-200-1,...,6   | $E = 4.0 \text{ kV/mm}$ ;<br>$t_p = 120 \text{ s}$               | $v = 4 \text{ V/s}$ ;<br>$I_{\text{max}} = 1 \mu\text{A}$ | ++       | Reproducibility of $A_d$ ;<br>reproducibility of final I–V curves               |
| 2.2   | 2-200-7,...,13  | $E = 4.5 \text{ kV/mm}$ ;<br>$t_p = 10\text{--}180 \text{ s}^a$  | $v = 4 \text{ V/s}$ ;<br>$V_{\text{max}} = 500 \text{ V}$ | ++       | $A_d = f(t_p) @ E = 4.5 \text{ kV/mm}$ ;<br>reproducibility of final I–V curves |
| 3.1   | 3-300-1,...,6   | $E = 4.67 \text{ kV/mm}$ ;<br>$t_p = 120 \text{ s}$              | $v = 4 \text{ V/s}$ ;<br>$I_{\text{max}} = 1 \mu\text{A}$ | ++       | Reproducibility of final I–V curves   |
| 3.2   | 3-300-7,...,13  | $E = 4.67 \text{ kV/mm}$ ;<br>$t_p = 10\text{--}180 \text{ s}^a$ | –   | +–       | $A_d = f(t_p) @ E = 4.67 \text{ kV/mm}$   |

<sup>a</sup>Concrete  $t_p$ -values: 10, 20, 30, 60, 90, 120, and 180 s.

The 325-nm-UV-laser light generates an influx of charge carriers at the illuminated spot and, thus, lowers the coercive field locally significantly to only 20% of the value in darkness (the general phenomenon had been reported earlier<sup>34</sup>). Therefore, a

significantly lower electric field of 3.5 kV/mm at the spot is required to initiate the inversion of polarization. This field was generated by an Agilent 33220A arbitrary waveform generator, whose output was amplified by two different HV amplifiers: (a) A Matsusada

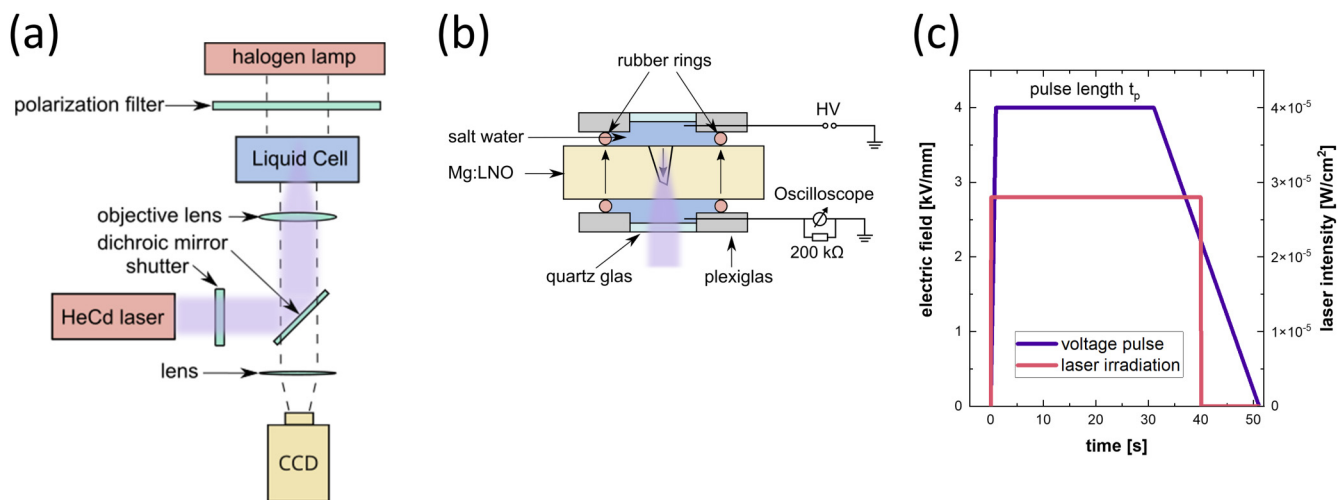


**FIG. 1.** Schematics illustrating the growth of hexagonal ferroelectric domains in  $\text{LiNbO}_3$  single crystals: (a) Overview picture of the optical setup: A HeCd laser with a wavelength of 325 nm acts as the UV-light source. Utilizing various optical lenses and an inverted microscope, the UV light, which lowers the coercive field on the one hand and provides positional control of the domain growth on the other hand, is focused on the top of the sample in a home-built liquid cell. The laser exposure time is precisely set by a computer-controlled shutter. A halogen lamp with a linear polarization filter illuminates a CCD camera through the crystal, allowing *in situ* observation of the growing domains. (b) Sketch of the liquid cell with the electronic circuit for monitoring and adjusting an applied electric field with a pulse generator multiplied by a high-voltage amplifier (HV). (c) Diagram of an exemplary poling recipe, showing the poling field (violet line) and laser irradiation (red line) applied to the samples. Immediately upon the start of a poling procedure, laser irradiation begins at  $2.8 \times 10^{-5} \text{ W/cm}^2$ , and the electric field  $E$  is increased to 4 kV/mm over a period of 1 s. For the next period— $t_p = 30 \text{ s}$ —the electric field and laser irradiation are kept constant. Afterward, the electric field is slowly, linearly decreased to zero over  $t_{\text{rampdown}} = 20 \text{ s}$  to minimize any spontaneous back-switching effects. During this process, the laser irradiation is switched off when the electric field reaches half of its original value. Refer also to Sec. B/Fig. S1 of the [supplementary material](#) for information on the development of typical switching currents during the process.

24 September 2024 11:46:39

Precision AMT-20B10-LC(230 V) HV amplifier with a maximum output current of  $\pm 10$  mA, a maximum voltage of 20 kV, and a slew rate of up to 360 V/ $\mu$ s, and (b) using a Trek 2210 with a maximum output current of  $\pm 20$  mA, a maximum voltage of 1 kV, and a slew rate of up to 150 V/ $\mu$ s. We noticed no differences in the poling process and kinetics in the overlapping voltage range of the two HV amplifiers. Additionally, we monitored the voltage pulse as well as the poling current by a Tektronix TDS2024B digital oscilloscope.

In addition, the *in situ* nucleation and growth of domains were monitored in real-time using a white-light polarization microscope illuminating the sample from the top and a CCD camera. Diffraction-limited domain tracking was, thus, possible due to the strain-induced birefringence close to DWs. Samples were fixed onto the microscope in a custom-built liquid cell sample holder, sketched in Fig. 1(b). The liquid cell itself consists of two plexiglas parts having a quartz glass window in their center to ensure the optical transmission of UV light. The sample was held in place between two rubber O-rings acting as spacers, while the surrounding cell volume on both sample sides was filled with a 2 wt. % NaCl solution. These “liquid electrodes” ensure transparency while providing a uniform electric field distribution across the whole sample surface.<sup>37</sup> An analysis of domain area  $A_d$  as a function of NaCl concentration was performed in a second preliminary experiment that is reported in Sec. I of the [supplementary material](#), using sample batch 1.5, and showing the independence on  $A_d$  over a broad range of NaCl-concentrations.

To ensure reproducibility, the poling experiments were always carried out by following the same sequences of sample treatment:

- (i) A fresh sample was extracted from a LN wafer and
- (ii) subjected to a thorough cleaning procedure that included a 10-min oxygen-plasma etching step (1.0 mbar  $O_2$ -pressure, ATTO Low-Pressure Plasma System 200 W, 40 kHz, Diener Electronic GmbH & Co KG) followed by a 5-min ultrasonic cleaning each in acetone and isopropanol, and, finally, rinsed with de-ionized water.
- (iii) Each sample was mounted onto the liquid cell with a NaCl solution for domain poling, with the z+ side always facing upward. Equally, the laser entered the sample by the z-side and was focused onto the z+ interface.
- (iv) The subsequent *poling protocol* is shown in Fig. 1(c): At the beginning, a sharp voltage ramp was applied lasting for 1 s until it reached the maximum electric field. Then, the selected maximum poling voltage was kept constant for a certain pulse length  $t_p$ . To terminate the poling process, the electric field was slowly lowered over a time period of  $t_{\text{rampdown}} = 20$  s to minimize the effects of spontaneous back-switching.<sup>38</sup> Throughout the poling process, the sample was constantly irradiated until 10 s to the end, as the applied electric field reached a value lower than half of the coercive field  $E_c$ .
- (v) Every freshly grown domain was subsequently imaged by polarization light microscopy (PLM), and the grown domain area  $A_d$  was extracted from measurements of the hexagon's side lengths. Therefore, the full area inside the hexagon was considered, ignoring occasionally and spontaneously appearing back-switched small inner domains for the sake of standardization. In selected cases (samples 1–3 of batch 2.1 and all samples of

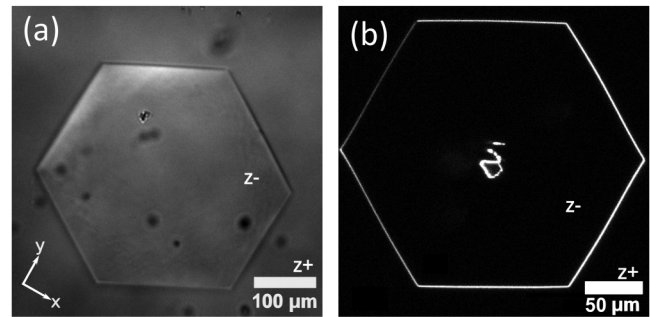


**FIG. 2.** Image of the domain in sample 2-200-17 under (a) a polarization-sensitive light microscope (PLM) and (b) a second-harmonic generation microscope (SHGM). For further details on both imaging methods and the extraction of the domain area, see Secs. C–F in the [supplementary material](#).

batches 1.2, 1.3, 2.2, 3.1, and 3.2), 3D images of the full DW morphology were collected by second-harmonic generation microscopy (SHGM). An elaborate comparative description of both imaging methods (see Fig. 2 for typical results) as well as the mathematical details on domain area determination is given in Secs. C–F of the [supplementary material](#).

- (vi) After the PLM image acquisition, all samples underwent the above cleaning protocol once more, however, starting with an initial de-ionized-water rinsing step to eliminate any salt residues.
- (vii) Finally, 10-nm-thin chromium electrodes were vapor-deposited under high-vacuum conditions (base pressure of  $10^{-6}$  mbar) onto both sides of the LN crystals using a  $3 \times 3$  mm<sup>2</sup> shadow mask that fully covers the newly grown domain. This ensures proper electrical contacts to DWs for both current–voltage (I–V) recording and DWC enhancement through high-voltage (HV) ramping.

24 September 2024, 11:46:39

### C. Current-voltage (I–V) characterization and a DWC enhancement procedure

The vision for the investigated DWs is their application in various electronic commercial devices—thus, current–voltage (I–V) dependence and its predictability are the clue characteristics to be evaluated. In this work, we recorded I–V curves of all DWs at three stages of production: directly after domain growth by UV-assisted poling, during the DWC enhancement process by HV ramping, and after HV ramping. The above-mentioned Cr electrodes were, therefore, connected to a Keithley 6517B electrometer using metal wires and conductive silver paint. The electrometer was used twofold: first, to record the macroscopic I–V data and second, as the HV source to carry out the DWC enhancement procedure. I–V curves between  $-10$  V and  $+10$  V and voltage increments of  $\delta V = 0.5$  V with  $\delta t = 2$  s were acquired both before and after enhancement. Each of the I–V curves was measured over multiple cycles until the respective curve showed a stable shape. Then, the measurement was aborted, and only the last acquired stable cycle was considered for further evaluation (exemplarily refer to Fig. S9 in Sec. K of the [supplementary material](#) for complete I–V-curve cycles obtained for batch 2.1).

DWC enhancement was carried out based on the protocol as introduced by Godau *et al.*<sup>16</sup> the  $-z$ -electrode of every sample is set to ground, and a negative voltage is applied to the  $+z$ -side (with respect to the original monodomain crystal), increasing linearly at a rate of  $v = 4 \text{ V/s}$  up to a value  $V_{\text{max}}$  that corresponds to 60% of  $E_C$  and, hence, up to  $3.3 \text{ kV/mm}$ .<sup>22</sup> In the following, the as-summarized DWC-enhancement procedure will be referred to as “voltage-limited.” Initially, i.e., for batches 1.2, 1.3, and 2.2, voltage ramps up to  $V_{\text{max}} = 500 \text{ V}$  were applied, but this led to the disintegration of the original domain structure into smaller fragmented regions containing numerous tiny needle-like spike domains, named hereafter as “exploded” domains—a phenomenon, which had been described for a single LN sample by Kirbus *et al.*<sup>22</sup> earlier. Notably, during this procedure, a sudden current jump from  $10^{-5} \text{ A}$  to  $10^{-3} \text{ A}$  was observed.

To address this “explosion” issue, we improved the DWC-enhancement procedure by stopping voltage ramping whenever a maximum current  $I_{\text{max}}$  of  $10^{-6} \text{ A}$  is reached and keeping the corresponding voltage value constant subsequently. This type of DWC enhancement is labeled “current-limited” hereafter. Notably, the *current-limited* regime preserves the domain structure and size in the sense of “ex-/implosion-prevention” in the majority of cases investigated here. Hence, all subsequent DWC-enhancement procedures were carried out using this improved approach, in particular, with sample batches 2.1 and 3.1.

As a quick overview, Table I summarizes for which sample batch I–V data have been acquired and under which circumstances (stopping by reaching  $V_{\text{max}}$  or  $I_{\text{max}}$ ) the “enhancement” procedure was carried out.

### III. RESULTS AND DISCUSSION

#### A. Reproducibility and tunability of the as-grown domain area

In this part, the domain engineering method of UV-assisted liquid-electrode poling is investigated with respect to the impact of

several process parameters (poling pulse duration  $t_p$ , electrical field strength  $E$ , wafer type) on the final domain area  $A_d$  and the I–V characteristics of its DW, while a detailed description of the growth process itself, as (i) known from the literature and (ii) derived from a SHGM investigation of the DW inclination as a function of the poling pulse length  $t_p$ , is summarized in Sec. G of the [supplementary material](#).

#### 1. Domain area as a function of poling pulse duration, electrical field, and wafer type

To gain an understanding of the domain areas’ dependence on the poling time  $t_p$ , we performed several series of measurements with  $t_p$  being varied between 10 and 180 s for the sample batches 1.2 (dark blue), 1.3 (violet), 2.2 (red), and 3.2 (gold), as plotted in Fig. 3(a). In addition, we varied the electric field strength  $E$  and compared samples between the three LN wafers.

Regardless of the field strength or the wafer type, the dependence of the poling duration  $t_p$  on the domain area always shows the same trend: a sharp increase in size at short poling times slowly flattens out the longer the poling process takes. This behavior can be attributed to laser irradiation—the area surrounding the laser spot maintains a significantly lower coercive field as compared to distant regions, facilitating a faster growth rate and DW propagation speed. When the coercive field increases due to a lower number of free charge carriers in less illuminated areas, the expansion slows down until it reaches a stable growth rate. As reported in the literature, the growth rates in the undisturbed regions of the crystal were steady at a constant electric field.<sup>39,40</sup>

To further investigate the growth parameters, the same measurement series was carried out with an increased electric field of  $4.5 \text{ kV/mm}$ . This led to a faster domain growth, and the domain area increased by 42% in comparison with the previous measurement series on the same wafer. The overall trend did not change, with a slowing down of the expansion speed as the poling length increased.

24 September 2024, 11:46:39

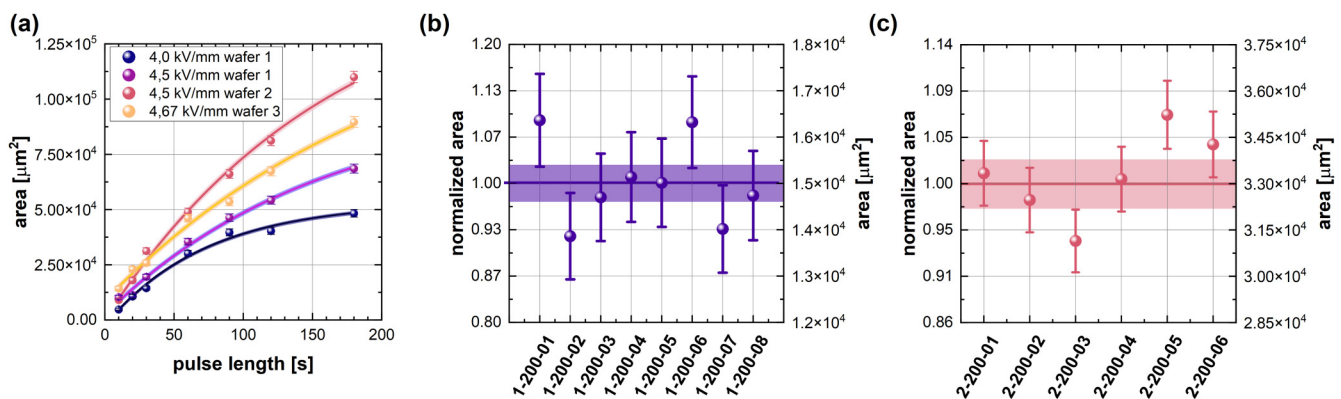


**FIG. 3.** (a) To investigate the dependence of the domain area on the poling-voltage pulse duration, we varied  $t_p$  between 10 and 180 s. This resulted in an increase of the domain area of one order of magnitude between the shortest and longest pulse. Furthermore, three different electric fields, as well as samples from three different wafers, were investigated. Noticeable size differences were found between the sample batches of the different wafers. (b) and (c) To probe the reproducibility of the created domain area, two measurement series of domains fabricated with the same poling recipe were carried out. One series with  $t_p = 30 \text{ s}$  for samples from wafer 1 in (b) and another series with  $t_p = 120 \text{ s}$  for samples originating from wafer 2 in (c). The solid horizontal lines indicate the mean area reached with this particular poling protocol, respectively.

An equivalent measurement series was performed with samples from wafers 2 and 3 with similar electric field strength, as also pictured in Fig. 3(a). Surprisingly, we found significant differences in growth rates between all three wafers. The samples from wafer 2 [red dots in Fig. 3(a)] exhibited the fastest growth. In contrast, the samples from wafer 1 (violet) grew the slowest, even though they underwent the same poling protocol. The thicker samples from wafer 3 (gold) were poled with a slightly higher electric field but still reached a comparable growth speed as the other specimens. We attribute these discrepancies to dissimilar defect and impurity distributions, leading to different amounts of pinning events for DWs and, thus, slightly varied growth rates.<sup>38</sup> As a practical conclusion, a careful *calibration* of growth speeds is required to achieve domains of comparable sizes, in particular, when samples are produced from different wafers—even if the latter have nominally the same chemical composition.

## 2. Size variations for virtually equally grown hexagonal domains

The goal of these experiments was to examine the reproducibility of the domain size within the UV-assisted liquid-electrode poling process. A series of eight samples from wafer 1 with a  $t_p = 30$  s (batch 1.1) and six samples from wafer 2 with a  $t_p = 120$  s (batch 2.1) were prepared and the domain areas exemplarily compared, as shown in Figs. 3(b) and 3(c). The shorter pulse duration  $t_p = 30$  s, as illustrated in Fig. 3(b), resulted in a smaller area of  $1.5 \times 10^4 \mu\text{m}^2$  with a deviation of 7%. In contrast, the longer pulse duration, as shown in Fig. 3(c), yielded an area of  $3.25 \times 10^4 \mu\text{m}^2$  with a deviation of 9%. All domains exhibited a hexagonal shape, as depicted in Fig. 2, characterized by one pair of slightly longer parallel sides,

which can be attributed to the pinning of the domain wall and the weakly oval shape of the laser spot. Overall, we conclude that this poling method is capable of creating domains of the same size with a reasonable uncertainty. Potentially, variations may be reduced further if some form of *in situ* control of the domain size, i.e., by machine vision via PLM, is applied.

## 3. Electrical characterization of as-grown domain walls

Current–voltage (I–V) characteristics in the  $\pm 10$ -V-range were systematically collected in the initial as-grown (as-poled) state and after the conductivity-“enhancement” procedure. For the first case, we present the I–V characteristics of samples from batches 2.1 and 3.1 in Fig. 4. The two batches exhibit qualitatively similar characteristics with clear non-linear behavior, asymmetry with respect to voltage polarity (as discussed and explained in Ref. 18), and occasionally pronounced electrical noise due to the low current magnitude, which can be seen, especially, well in Fig. 4(b). The maximum absolute current, acquired at  $\pm 10$  V for all samples in batches 2.1 and 3.1, falls within the range of  $4.3 \times 10^{-13}$  to  $2.4 \times 10^{-10}$  A for a  $-10$  V bias voltage, and  $1.1 \times 10^{-13}$  to  $2.6 \times 10^{-12}$  A at  $+10$  V. These values are already very close to the bulk conductivity of LN and correspond to a typical insulator rather than a conductive domain wall.

Notably, when subjected to the maximum positive voltage, the sample conductance is lower as compared to that under a negative voltage of equivalent absolute magnitude, with a narrower dispersion of values among the samples, as is evident from Figs. 4 and 6.

The I–V curves of identically prepared samples prior to DWC “enhancement” exhibit significant variations in magnitude. Given that the production parameters were consistent among all samples,

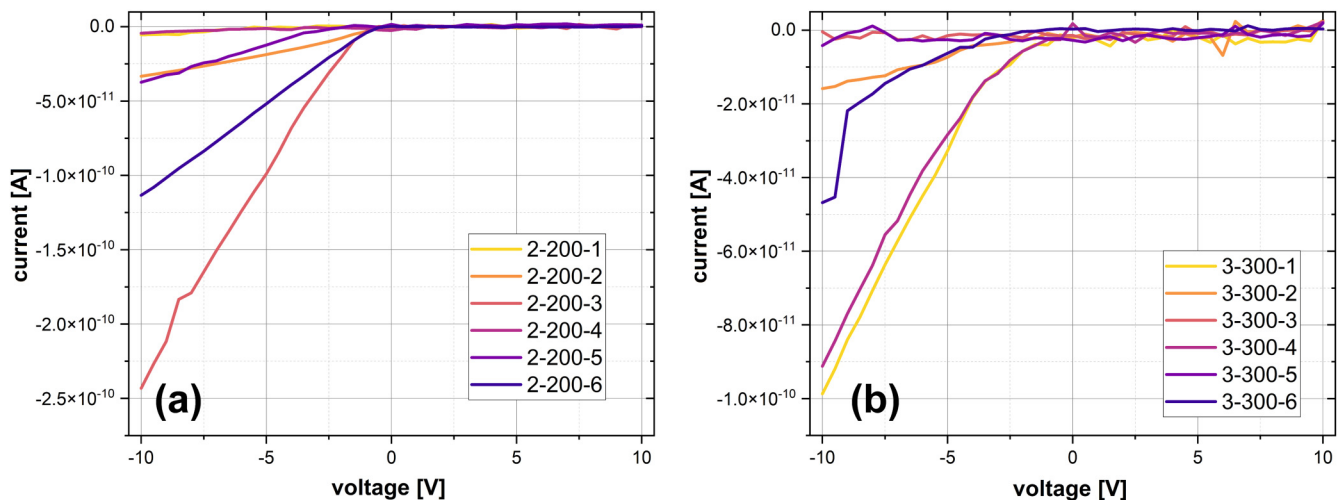


**FIG. 4.** Current–voltage curves of the samples from batches 2.1 (a) and 3.1 (b) directly after poling, before any further modification of the domain wall structure took place. As can be seen from the diagrams, the initial conductance is different for the samples after poling under identical conditions, which stresses the influence of individual lattice defects in the vicinity of the domain walls and different real structures of the DW-electrode contacts. Currents at negative voltages are significantly higher than at positive ones – a phenomenon, which has been described previously.<sup>18</sup> According to the used Keithley 6517B electrometer specifications sheet,<sup>41</sup> uncertainty for the measured current values is equal to 1%.

24 September 2024 11:46:39

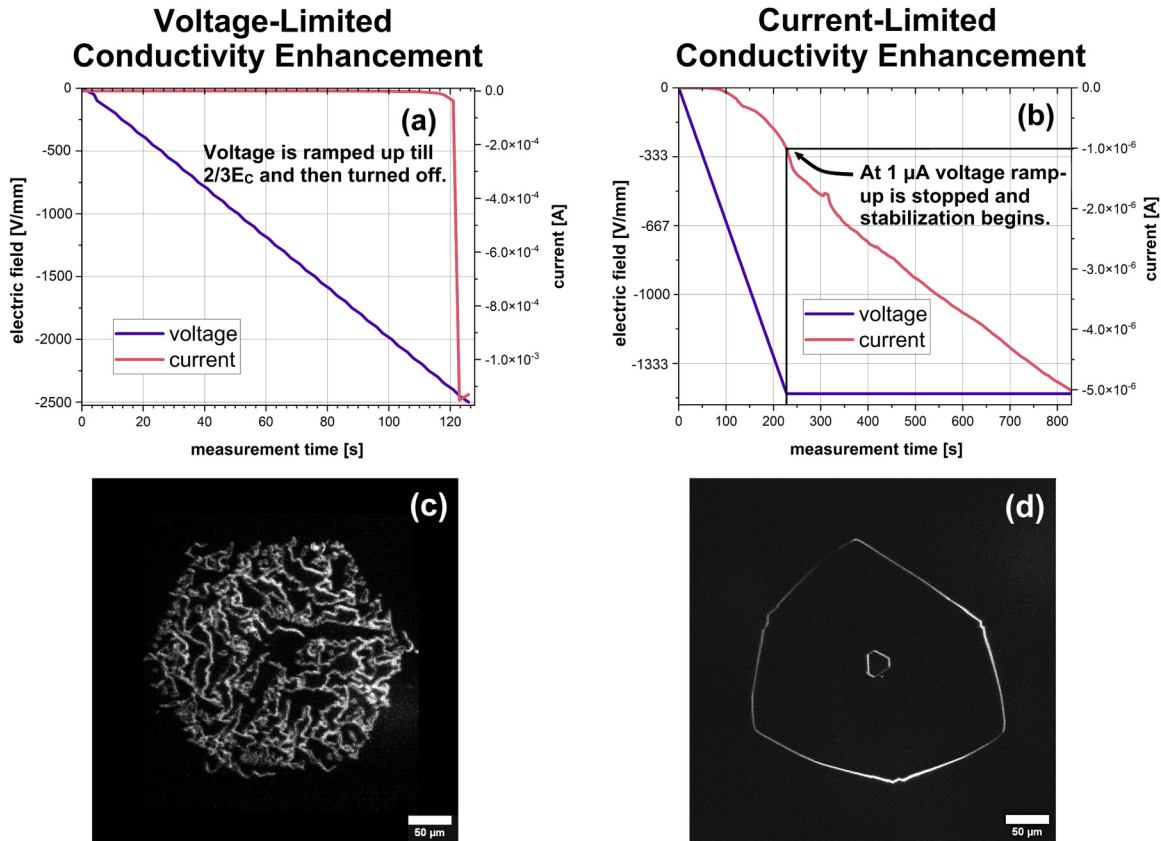


**FIG. 5.** The I–V characteristics during the DWC-enhancement process for the *voltage-limited* (a) and the *current-limited* (b) approaches, illustrated alongside the resulting DW structures [(c) and (d)], as imaged by SHGM, of samples 2-200-11 and 3-300-3, respectively. In the first case, a negative voltage is applied to the  $z^+$  side of the LN DW sample, gradually increasing at a rate of 4 V/s until reaching 500 V. A subsequent 10-min stabilization occurs at the maximal voltage. The corresponding plot (a) depicts a swift surge in the current (by more than one order of magnitude) during the voltage ramp-up, resulting in an “imploded” geometrical domain structure (c). This phenomenon was observed across 21 domains of varying sizes with the current rapidly increasing after reaching a value of  $10^{-5}$  A in all cases. In an improved version of procedure (b), the voltage ramp-up at 4 V/s was terminated once the current achieved  $10^{-6}$  A, with a 10-min stabilization period. As evident from plot (b), this modification eliminates the rapid current increase, leading to DWs with a regular geometrical shape (d) in the majority of cases. For the range of current values, presented in the above graphs, the uncertainty is equal to 0.1%.<sup>41</sup>

we hypothesize that these electrical disparities may be attributed to local defects and impurities within the crystal lattice, particularly, those present near or at the sample surface. This hypothesis is supported by previous findings,<sup>16,18</sup> which established that the geometrical and electronic real structure of the interface between the crystal and electrode serves as a crucially determining factor for charge transport.

## B. Reproducibility of the I–V characteristics after domain wall conductivity enhancement procedures

In this part, the conductivity enhancement of domain walls by high-voltage ramping and the reproducibility of the resulting I–V characteristics are examined. This encompasses the application of the protocol proposed by Godau *et al.*,<sup>16</sup> the subsequent refinement toward a *current-limited* approach, and the characterization

of the obtained highly conductive DWs (compared to as-poled DWs) by both I–V measurements and second-harmonic generation microscopy.

### 1. Voltage- vs current-limited domain wall conductivity enhancement

Immediately after the I–V characterization of as-poled DWs, the DWC enhancement procedure,<sup>16</sup> as described in detail in Sec. II C, was applied to the samples of batches 1.2, 1.3, and 2.2. In this original, so-called *voltage-limited* protocol, the maximal pre-defined value of the voltage was +500 V for 200  $\mu\text{m}$  thick samples, followed by a 10-min stabilization period under the application of the maximal voltage. Throughout this process, a sharp current surge from  $10^{-5}$  to  $10^{-3}$  A at 200 V was consistently observed for all the samples [exemplified by Fig. 5(a)], which cannot be



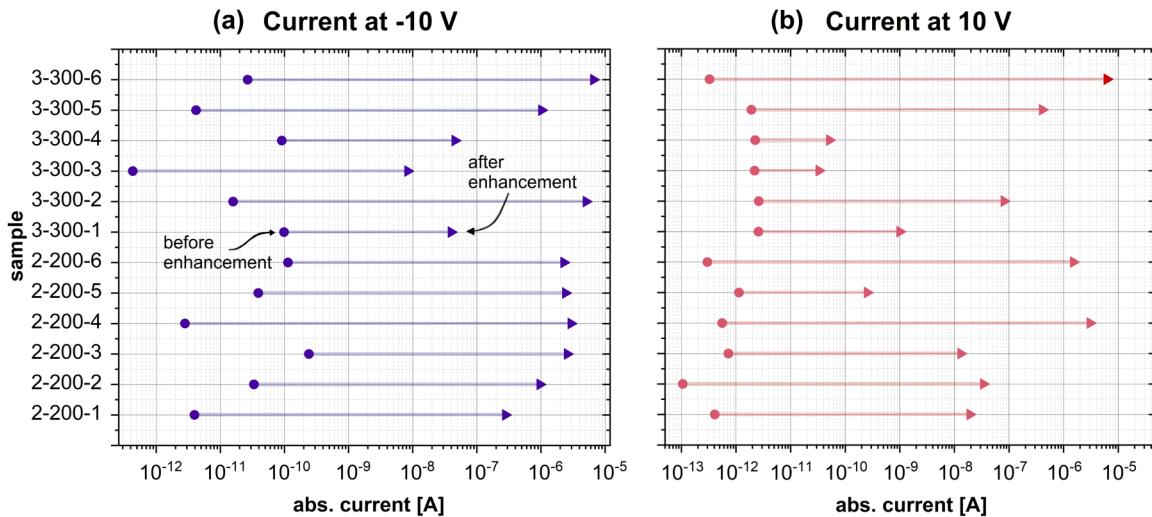


**FIG. 6.** Change of the DW current at  $\pm 10$  V (red and violet signs, respectively) for the 12 samples of batches 2.1 and 3.1 before (dots) and after (triangles) the DWC enhancement procedure. The magnitudes of current change span from approximately one order of magnitude (sample 3-300-3 at  $-10$  V) to more than seven orders of magnitude (sample 3-300-6 at  $-10$  V). On average, the current at  $+10$  V increases by five orders of magnitude and at  $-10$  V by six orders of magnitude. For the majority of cases, the current under a positive measuring voltage is larger both before and post-enhancement. The full I-V curves can be found in Fig. S8 of the [supplementary material](#).

interpreted solely as a switching current due to the following quantitative estimation: The current peak in Fig. 5(a) lasts around 3 s with an amplitude of 1 mA, which results in a total charge of at least 3 mC flowing through the circuit. In contrast, a full back-switching of the corresponding domain in Fig. 5(c), which has an area  $A_d$  of around  $7 \times 10^{-4} \text{ cm}^2$ , requires only a charge of  $2P_s A_d \approx 0.1 \mu\text{C}$  (with  $P_s = 71 \mu\text{Ccm}^{-2}$  being the spontaneous polarization for LN<sup>42</sup>), which is more than four orders of magnitude lower. Thus, it can be concluded that the main part of the current peak corresponds to the successfully increased DW conductivity. The analysis of corresponding SHGM images of these domains unveiled the disintegration of singular hexagonal domains into numerous minute needle-like domains, as depicted in Fig. 5(c). This abrupt current increase obviously caused a domain “implosion,” i.e., the fracturing into many needle-like structures, which makes this process uncontrollable and irreversible.

Hence, to achieve a more homogeneous geometrical “enhancement” result, the current-limited scheme was applied to batches 2.1 and 3.1, where each domain wall is voltage-treated until a maximum current value is reached, instead of a predefined target voltage. To achieve this, the increase in voltage was immediately halted as soon as the current reached the level of  $10^{-6}$  A, which is an order of magnitude smaller than the critical threshold of  $10^{-5}$  A, where the “implosion” was observed, providing a safety margin. The changes in both current and voltage during the procedure are plotted in Fig. 5(b), while the corresponding SHGM image, showcasing an exemplary conductivity-enhanced domain wall, is displayed in Fig. 5(d). It is evident that the current exhibited a rather smooth transition throughout the procedure, resulting in the formation of domain shapes with a regular triangular pattern, as previously described.<sup>16</sup>

## 2. Current-limited DWC enhancement: Final electrical performances and domain wall shapes

The—in terms of geometrical reproducibility favorable—current-limited domain wall conductivity enhancement procedure was performed on a statistically significant number of 12 samples (batches 2.1 and 3.1), which exhibit after-poling hexagonal domains of approximately similar sizes of  $270 \mu\text{m}$  in diameter. Although the DWC enhancement procedures were executed under uniform conditions, there exists still a notable distinction in the I-V characteristics observed during and after the enhancement process across all samples. For a visual representation of this variance refer to Fig. 6, where the DW samples are compared with respect to the maximal currents obtained at  $\pm 10$  V, as well as to Fig. S8 in the [supplementary material](#), where the corresponding I-V raw data are provided.

When comparing the current-voltage characteristics before and after the conductivity enhancement process among samples from the same batch, such as six samples from wafer 2 (samples 2-200-1, . . . ,6) and six samples from wafer 3 (samples 3-300-1, . . . ,6), a significant difference in pre- and post-enhancement conductance is evident; see Fig. 6. A clear current enhancement was observed in all cases, with the maximal factor of  $1.9 \times 10^7$  (sample 3-300-6 at  $+10$  V) and a minimal enhancement factor of 15 (sample 3-300-3 at  $+10$  V). Both of them are outliers in terms of their magnitude, while the average enhancement factors are  $1.7 \times 10^5$  for  $-10$  V and  $2.5 \times 10^6$  for  $+10$  V. Despite their identical preparation and DWC-enhancement procedures, the conductance of these samples varies notably, sometimes even by multiple orders of magnitude. The SHGM images obtained *after* the enhancement process explain these conductance disparities to

some extent since they unveil corresponding variations in the geometrical structures of the domain walls. Some samples still display an “imploded” state [e.g., sample 3-300-6; see Figs. 7(j) and 7(k)], even though the voltage ramp was halted after reaching a current value of  $10^{-6}$  A. Conversely, other samples exhibit random, highly irregular structures that differ significantly from each other [see Figs. 7(d), 7(g), and 7(e)] and cannot be categorized as being imploded. Notably, the current–voltage relationship during the conductivity enhancement procedure varies noticeably from the outset. This is evident from the voltage and time dependences of

current during the procedure [Figs. S8(a) and S8(d) of the [supplementary material](#)]. For instance, the current of samples 2-200-3 and 2-200-4 differs by two orders of magnitude at a low voltage of 25 V during enhancement. Similarly, the maximal stabilization voltages can span from  $-308$  V to  $-478$  V [Fig. S8(d) in the [supplementary material](#)]. The decisively varying DW geometries are accompanied by substantial differences in the resulting *post-enhancement* I–V characteristics [Figs. 7(c), 7(f), 7(i), and 7(l)]. Here, we see how the maximal current differs by up to three orders of magnitude between the investigated samples, while the curves also

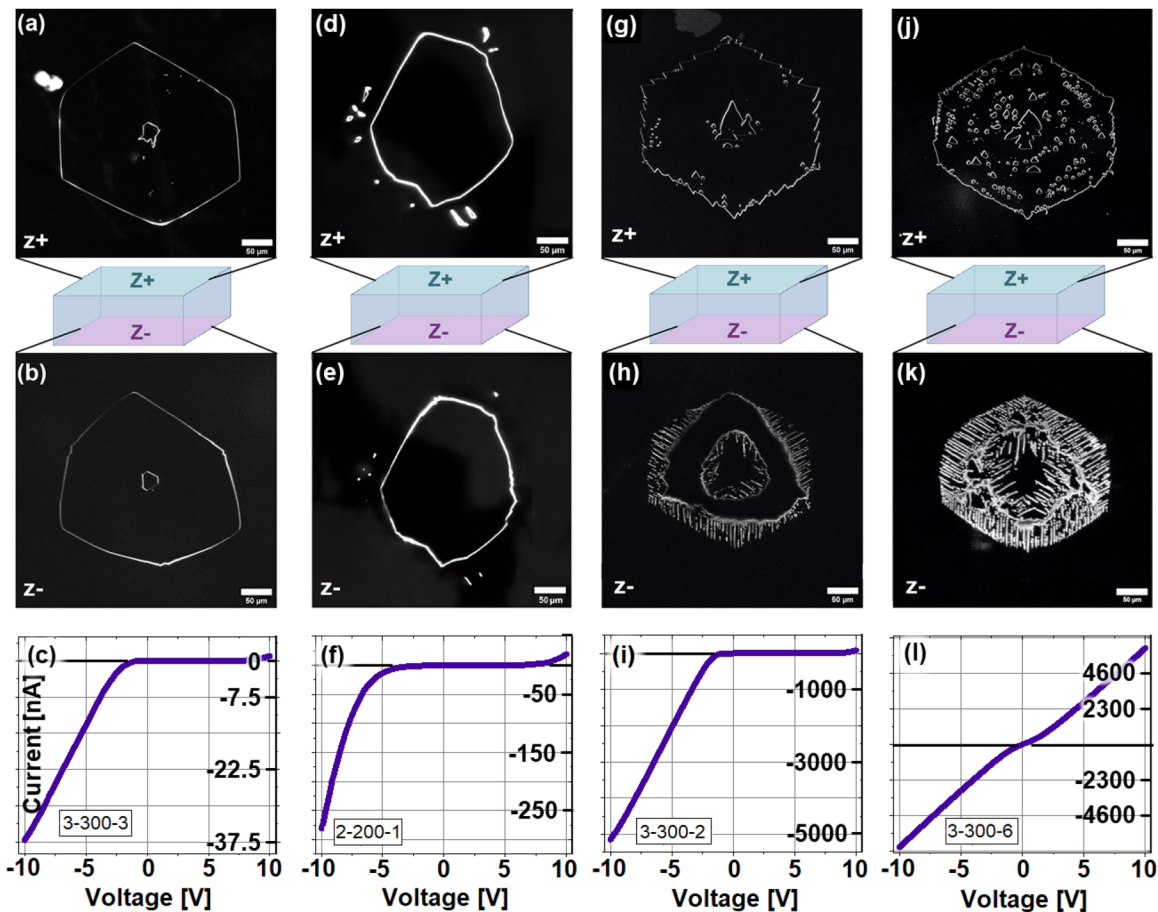


**FIG. 7.** Domain SGHM images at both +z- and –z- sides of the samples 3-300-3 (a) and (b), 2-200-1 (d) and (e), 3-300-2 (g) and (h), and 3-300-6 (j) and (k), correspondingly, taken after the DWC-enhancement process using the current-limited scheme. As can be seen from the selection of images, the geometrical form of the domains can still vary substantially; from the already described<sup>16</sup> “triangular” shape of the domain like in the case of the sample 1-300-3, to the shape of the irregular oval in the case of the sample 2-200-1, where no symmetry in relation to the crystal axes can be traced, toward the cases of the two other samples (3-300-2 and 3-300-6) exhibiting several stages of spike domain formation. In the latter two cases, the residual pinning sites, which appeared during the conductivity enhancement procedure, are clearly visible on the –z-side of the crystal (and through all of the crystal bulk as well), while such an effect is not visible in the case of the sample 3-300-3, prepared from the very same wafer, meaning that the chemical differences or defect concentration could hardly play any role. The sample 3-300-6 can also be characterized as imploded, while sample 3-300-2 demonstrates only several spike domains inside the poled domain and, thus, presents the early stage of a DW implosion. Panels (c), (f), (i), and (l) show the resulting I–V characteristics. The substantial differences in the geometrical structure are tightly intertwined with significant differences in the I–V curves; the current levels between samples can vary up to two orders of magnitude; the measure of “non-linearity” from a sample to sample is also quite different, with sample 3-300-6 (k) demonstrating the least “rectifying” behavior. Note that for all the above presented I–V curves, the measurement uncertainty lies between 0.1 and 0.2%.<sup>41</sup>

exhibit quite different shapes (rectifying vs ohmic/linear), with the imploded sample 3-300-6 [Fig. 7(l)] being an outlier in terms of “linearity.” Furthermore, analysis of the rest of the samples does not allow us to extract an unambiguous correlation between the geometrical structure of the domain wall, in particular, its average inclination toward the  $z$ -axis, and its conductive properties yet—the differences, so far, appear to be random. These results point us toward inherent (local) variations within the nominally homogeneous crystal itself playing a decisive role, including the exact distribution of crystalline defects and impurities within both the bulk of the crystal and its surface, as well as the individual electronic defect structure of the DW-electrode junction.

The reasons behind the limited reproducibility in CDW production remain to be studied even more profoundly. From previous works, it was concluded that the shape of the inclined domain walls directly impacts their conductance,<sup>25</sup> which is linked to  $\sin(\alpha)$ , where  $\alpha$  represents the angle of the DW's inclination with respect to the crystal's  $z$ -axis. This inclination is sensitive to the surrounding electric fields, including external ones<sup>16,43</sup> and internal fields within the crystal, such as depolarization and defect fields.<sup>44,45</sup> The influence of external fields during DWC enhancement is still not thoroughly studied. The transformation of a hexagonal structure into a rounded triangle due to DWs contracting inwardly, except at three fixed points along the triple  $y$ -axis symmetry, as described by Kirbus *et al.*<sup>22</sup> and Godau *et al.*,<sup>16</sup> seems more an exception than a rule after this large scale study.

For instance, comparing the conductance of samples from two different wafers (Fig. 6—wafer 2 with a thickness of  $200\ \mu\text{m}$  and wafer 3 with a thickness of  $300\ \mu\text{m}$ )—reveals that CDWs in the thicker wafer tend to exhibit lower conductance (three out of six samples have a maximal current below  $0.1\ \mu\text{A}$ ; while for the thinner wafer, the maximum current for all samples was around  $1\ \mu\text{A}$ ). These differences could be explained by (i) slight variations in the chemical composition of the crystals and (ii) by potential differences in the electric field gradient during the enhancement procedure. For both batches, the voltage ramp-up was the same, resulting in an electric field gradient 1.5 times higher for the thinner samples of batch 2.1. One may hypothesize that the electric field gradient is directly connected to the final conductivity of the structures, which needs a systematic follow-up investigation.

Last, theoretical studies<sup>46,47</sup> highlight the high sensitivity of surface chemical and physical properties to the methods used in crystal production and the surrounding conditions. These aspects, in turn, influence geometry and, thus, the conductance of CDWs. Furthermore, experimental data from Kirbus *et al.*<sup>22</sup> indicate that the interface between CDW and metal electrode serves as the primary hindrance to charge transport due to the absence of DW inclination near the surface. This underscores the need for a more comprehensive investigation into the interface conditions between the crystal and the electrode, e.g., by varying the contact metal and the surface preparation protocol.

#### IV. SUMMARY AND OUTLOOK

In the first part of this work, a method for reproducible fabrication of hexagonal ferroelectric domain structures into 200 and  $300\ \mu\text{m}$ -thick 5 mol. % MgO-doped  $\text{LiNbO}_3$  single crystals was

presented. We used a 325 nm UV-light-assisted electric-field poling setup and studied a variety of parameters influencing the fabrication. From these, key parameters, such as electric field strength and poling pulse duration, were identified and controlled by a poling protocol. The resulting domain structures have been analyzed with polarization-sensitive as well as second-harmonic generation microscopy and evaluated with respect to the domain area and uniformity. The reproducibility of the protocol was tested for two different poling pulse lengths, and upon achieving this, the dependence of the domain area on poling pulse duration for different wafers and electric field strength was measured.

This connection varies among different wafers of nominally equal chemical composition, even when all the other parameters remain constant, which might indicate high sensitivity to defect density and makes a growth-parameters' calibration routine necessary as soon as samples from a different  $\text{LiNbO}_3$  wafer are used. Overall, the inclination of the freshly poled domains is small, and therefore, the resulting DWs have low electrical conductance.

In the second part of this work, in order to increase the average DW inclination and, thus, the DW conductivity, the method of Godau *et al.*,<sup>16</sup> where the as-grown DWs are exposed to high-voltage ramps, was applied to the domain structures. Initially, the voltage was steadily increased by 4 V/s to 500 V. All domains undergoing this protocol “imploded,” i.e., disintegrated into many needle-like subdomains, once the current exceeded a maximum of  $10^{-5}$  A. To prevent this implosion in the ensuing measurements, a maximal current of  $10^{-6}$  A was implemented, and the voltage ramp was stopped upon reaching this value, leading to a current-limited rather than a voltage-limited scheme.

The testing of this current-limited approach has revealed that despite the identical conditions during the conductivity enhancement process, both the geometry of the domain wall structures and their conductance still exhibit significant variations, although less than 50% of the cases show signs of implosion. For instance, the difference in the maximal conductance among the samples can vary by up to three orders of magnitude. Likewise, the geometrical structure of the domain walls still displays a certain diversity, including pinning sites or loss of symmetry in relation to the crystal structure.

The breadth of the obtained data emphasizes the necessity for further investigation and standardization of the DWC enhancement process, as well as research on the correlation between conductance and geometric changes throughout the procedure. In this regard, the implementation of *in situ* SHG during the enhancement process shows promise.<sup>22</sup> Additionally, a more comprehensive examination of the influence of intrinsic electric fields, particularly those on the surface of the lithium niobate crystal,<sup>22</sup> is essential. Such fields can be affected by various factors, including the electrode material, surface preparation, processing method, and chemical composition of the crystal—their systematic study will be subject to future research.

The results of this work are far from conclusive, as the (i) domain growth as well as the (ii) DWC enhancement procedure are highly dynamic processes sensitive to many local and nanoscopic influences, which do not easily succumb to a straightforward macroscopic description and modeling. On the contrary, this extensive work highlights the fact that besides application-based research on

memories, neural networks, or rewritable electronics, more fundamental studies on the interplay and dynamics of domains and domain walls with localized defects are mandatory, if ever the dream of true DW-based nanoscopic electronics should become real.

## SUPPLEMENTARY MATERIAL

See the [supplementary material](#) for a complete list of all samples; more information on the stages of the initial domain poling process, including the development of the switching current; in-depth information on domain (wall) imaging by PLM and SHGM, including the mathematical extraction of the correct domain area; details on the domain growth process during UV-assisted poling with particular focus on the development of DW inclination; results of preliminary experiments investigating the domain area's dependence on laser intensity and NaCl concentration during UV-assisted liquid-electrode poling; diagrams with the complete I–V characteristics of sample batches 2.1 and 3.1 *during* and *after* DWC enhancement; and exemplary I–V cycles to demonstrate the DWC stabilization behavior.

## ACKNOWLEDGMENTS

We acknowledge financial support by the Deutsche Forschungsgemeinschaft (DFG) through joint DFG–ANR project TOPELEC (Nos. EN 434/41-1 and ANR-18-CE92-0052-1), the CRC 1415 (ID: 417590517), the FOR 5044 (ID No. 426703838; <https://www.for5044.de>), as well as through the Dresden–Würzburg Cluster of Excellence on “Complexity and Topology in Quantum Matter”—ct.qmat (EXC 2147, ID No. 39085490). This work was supported by the Light Microscopy Facility, a Core Facility of the CMCB Technology Platform at TU Dresden. I.K.'s contribution to this project is also co-funded by the European Union and co-financed from tax revenues on the basis of the budget adopted by the Saxon State Parliament. Furthermore, we thank Thomas Gemming and Dina Bieberstein for their assistance in wafer dicing.

## AUTHOR DECLARATIONS

### Conflict of Interest

The authors have no conflicts to disclose.

## Author Contributions

Julius Ratzenberger and Iuliia Kiseleva contributed equally to this paper.

**Julius Ratzenberger:** Data curation (equal); Formal analysis (equal); Investigation (equal); Validation (equal); Visualization (equal); Writing – original draft (equal); Writing – review & editing (supporting). **Iuliia Kiseleva:** Data curation (equal); Formal analysis (equal); Investigation (equal); Validation (equal); Visualization (equal); Writing – original draft (equal); Writing – review & editing (supporting). **Boris Koppitz:** Investigation (supporting); Visualization (supporting). **Elke Beyreuther:** Funding acquisition (supporting); Methodology (supporting); Supervision (equal); Writing – review & editing (lead). **Manuel Zahn:** Formal analysis (supporting); Software (lead). **Joshua Gössel:** Investigation

(supporting). **Peter A. Hegarty:** Investigation (supporting); Visualization (supporting). **Zeeshan H. Amber:** Investigation (supporting); Visualization (supporting). **Michael Rüsing:** Conceptualization (equal); Funding acquisition (equal); Methodology (lead); Project administration (equal); Supervision (equal); Writing – review & editing (supporting). **Lukas M. Eng:** Conceptualization (equal); Funding acquisition (lead); Methodology (supporting); Project administration (equal); Resources (lead); Supervision (equal); Writing – review & editing (supporting).

## DATA AVAILABILITY

The data that support the findings of this study are available from the corresponding author upon reasonable request.

## REFERENCES

- 1R. Waser and A. Rüdiger, “Pushing towards the digital storage limit,” *Nat. Mater.* **3**, 81–82 (2004).
- 2Z. Wei, W. Chao, L. Jian-Wei, J. Jun, and J. An-Quan, “Erasable ferroelectric domain wall diodes,” *Chin. Phys. Lett.* **38**, 017701 (2021).
- 3Y. Qian, Y. Zhang, J. Xu, and G. Zhang, “Domain-wall  $p$ - $n$  junction in lithium niobate thin film on an insulator,” *Phys. Rev. Appl.* **17**, 044011 (2022).
- 4A. Suna, C. McCluskey, J. Maguire, K. Holsgrove, A. Kumar, R. McQuaid, and J. Gregg, “Tuning local conductance to enable demonstrator ferroelectric domain wall diodes and logic gates,” *Adv. Phys. Res.* **2**, 2200095 (2023).
- 5T. Kämpfe, B. Wang, A. Haußmann, L.-Q. Chen, and L. M. Eng, “Tunable non-volatile memory by conductive ferroelectric domain walls in lithium niobate thin films,” *Crystals* **10**, 804 (2020).
- 6P. Chaudhary, H. Lu, A. Lipatov, Z. Ahmadi, J. P. V. McConville, A. Sokolov, J. E. Shield, A. Sinitiskii, J. M. Gregg, and A. Gruverman, “Low-voltage domain-wall LiNbO<sub>3</sub> memristors,” *Nano Lett.* **20**, 5873–5878 (2020).
- 7J. P. V. McConville, H. Lu, B. Wang, Y. Tan, C. Cochard, M. Conroy, K. Moore, A. Harvey, U. Bangert, L.-Q. Chen, A. Gruverman, and J. M. Gregg, “Ferroelectric domain wall memristor,” *Adv. Funct. Mater.* **30**, 2000109 (2020).
- 8J. Sun, Y. Li, Y. Ou, Q. Huang, X. Liao, Z. Chen, X. Chai, X. Zhuang, W. Zhang, C. Wang, J. Jiang, and A. Jiang, “In-memory computing of multilevel ferroelectric domain wall diodes at LiNbO<sub>3</sub> interfaces,” *Adv. Funct. Mater.* **32**, 2207418 (2022).
- 9J. Lin, F. Bo, Y. Cheng, and J. Xu, “Advances in on-chip photonic devices based on lithium niobate on insulator,” *Photonics Res.* **8**, 1910–1936 (2020).
- 10A. Boes, B. Corcoran, L. Chang, J. Bowers, and A. Mitchell, “Status and potential of lithium niobate on insulator (LNOI) for photonic integrated circuits,” *Laser Photonics Rev.* **12**, 1700256 (2018).
- 11M. Zhang, C. Wang, P. Kharel, D. Zhu, and M. Loncar, “Integrated lithium niobate electro-optic modulators: When performance meets scalability,” *Optica* **8**, 652–667 (2021).
- 12M. Rusing, P. O. Weigel, J. Zhao, and S. Mookherjee, “Toward 3D integrated photonics including lithium niobate thin films: A bridge between electronics, radio frequency, and optical technology,” *IEEE Nanotechnol. Mag.* **13**, 18–33 (2019).
- 13D. Zhu, L. Shao, M. Yu, R. Cheng, B. Desiatov, C. J. Xin, Y. Hu, J. Holzgrafe, S. Ghosh, A. Shams-Ansari, E. Puma, N. Sinclair, C. Reimer, M. Zhang, and M. Lončar, “Integrated photonics on thin-film lithium niobate,” *Adv. Opt. Photon.* **13**, 242–352 (2021).
- 14R. S. Weis and T. K. Gaylord, “Lithium niobate: Summary of physical properties and crystal structure,” *Appl. Phys. A* **37**, 191–203 (1985).
- 15M. Manzo, F. Laurell, V. Pasiskevicius, and K. Gallo, “Lithium niobate: The silicon of photonics!,” in *Nano-Optics for Enhancing Light-Matter Interactions on a Molecular Scale*, edited by B. Di Bartolo and J. Collins (Springer Netherlands, Dordrecht, 2013), pp. 421–422.

- <sup>16</sup>C. Godau, T. Kämpfe, A. Thiessen, L. M. Eng, and A. Haußmann, "Enhancing the domain wall conductivity in lithium niobate single crystals," *ACS Nano* **11**, 4816–4824 (2017).
- <sup>17</sup>C. S. Werner, S. J. Herr, K. Buse, B. Sturman, E. Soergel, C. Razzaghi, and I. Breunig, "Large and accessible conductivity of charged domain walls in lithium niobate," *Sci. Rep.* **7**, 9862 (2017).
- <sup>18</sup>M. Zahn, E. Beyreuther, I. Kiseleva, A. Lotfy, C. McCluskey, J. Maguire, A. Suna, M. Rüsing, J. Gregg, and L. Eng, "Equivalent-circuit model that quantitatively describes domain-wall conductivity in ferroelectric LiNbO<sub>3</sub>," *Phys. Rev. Appl.* **21**, 024007 (2024).
- <sup>19</sup>I. Stolichnov, L. Feigl, L. J. McGilly, T. Sluka, X.-K. Wei, E. Colla, A. Crassous, K. Shapovalov, P. Yudin, A. K. Tagantsev, and N. Setter, "Bent ferroelectric domain walls as reconfigurable metallic-like channels," *Nano Lett.* **15**, 8049–8055 (2015).
- <sup>20</sup>A. Suna, O. E. Baxter, J. P. V. McConville, A. Kumar, R. G. P. McQuaid, and J. M. Gregg, "Conducting ferroelectric domain walls emulating aspects of neurological behavior," *Appl. Phys. Lett.* **121**, 222902 (2022).
- <sup>21</sup>Q. Xia and J. J. Yang, "Memristive crossbar arrays for brain-inspired computing," *Nat. Mater.* **18**, 309–323 (2019).
- <sup>22</sup>B. Kirbus, C. Godau, L. Wehmeier, H. Beccard, E. Beyreuther, A. Haußmann, and L. M. Eng, "Real-time 3D imaging of nanoscale ferroelectric domain wall dynamics in lithium niobate single crystals under electric stimuli: Implications for domain-wall-based nanoelectronic devices," *ACS Appl. Nano Mater.* **2**, 5787–5794 (2019).
- <sup>23</sup>E. Singh, H. Beccard, Z. H. Amber, J. Ratzberger, C. W. Hicks, M. Rüsing, and L. M. Eng, "Tuning domain wall conductivity in bulk lithium niobate by uniaxial stress," *Phys. Rev. B* **106**, 144103 (2022).
- <sup>24</sup>J. R. Maguire, C. J. McCluskey, K. M. Holsgrove, A. Suna, A. Kumar, R. G. P. McQuaid, and J. M. Gregg, "Ferroelectric domain wall p-n junctions," *Nano Lett.* **23**, 10360–10366 (2023).
- <sup>25</sup>B. Wolba, J. Seidel, C. Godau, A. Haußmann, and L. Eng, "Resistor network modeling of conductive domain walls in lithium niobate," *Adv. Electron. Mater.* **4**, 1700242 (2017).
- <sup>26</sup>S. Y. Xiao, T. Kämpfe, Y. M. Jin, A. Haußmann, X. M. Lu, and L. M. Eng, "Dipole-tunneling model from asymmetric domain-wall conductivity in LiNbO<sub>3</sub> single crystals," *Phys. Rev. Appl.* **10**, 034002 (2018).
- <sup>27</sup>C. J. McCluskey, M. G. Colbear, J. P. McConville, V. S. J. McCartan, J. R. Maguire, M. Conroy, K. Moore, A. Harvey, F. Trier, U. Bangert, A. Gruverman, M. Bibes, A. Kumar, R. G. P. McQuaid, and J. M. Gregg, "Ultra-high carrier mobilities in ferroelectric domain wall Corbino cones at room temperature," *Adv. Mater.* **34**, 2204298 (2022).
- <sup>28</sup>M. Campbell, J. McConville, R. McQuaid, D. Prabhakaran, A. Kumar, and J. Gregg, "Hall effect in charged conducting ferroelectric domain walls," *Nat. Commun.* **7**, 13764 (2016).
- <sup>29</sup>P. Turner, J. McConville, S. McCartan, M. Campbell, J. Schaab, R. McQuaid, A. Kumar, and J. Gregg, "Large carrier mobilities in ErMnO<sub>3</sub> conducting domain walls revealed by quantitative Hall-effect measurements," *Nano Lett.* **18**, 6381–6386 (2018).
- <sup>30</sup>H. Beccard, B. Kirbus, E. Beyreuther, M. Rüsing, P. Bednyakov, J. Hlinka, and L. M. Eng, "Nanoscale conductive sheets in ferroelectric BaTiO<sub>3</sub>: Large Hall electron mobilities at head-to-head domain walls," *ACS Appl. Nano Mater.* **5**, 8717–8722 (2022).
- <sup>31</sup>H. Beccard, E. Beyreuther, B. Kirbus, S. D. Seddon, M. Rüsing, and L. M. Eng, "Hall mobilities and sheet carrier densities in a single LiNbO<sub>3</sub> conductive ferroelectric domain wall," *Phys. Rev. Appl.* **20**, 064043 (2023).
- <sup>32</sup>C. L. Sones, M. C. Wengler, C. E. Valdivia, S. Mailis, R. W. Eason, and K. Buse, "Light-induced order-of-magnitude decrease in the electric field for domain nucleation in MgO-doped lithium niobate crystals," *Appl. Phys. Lett.* **86**, 212901 (2005).
- <sup>33</sup>M. C. Wengler, B. Fassbender, E. Soergel, and K. Buse, "Impact of ultraviolet light on coercive field, poling dynamics and poling quality of various lithium niobate crystals from different sources," *J. Appl. Phys.* **96**, 2816–2820 (2004).
- <sup>34</sup>H. Steigerwald, F. von Cube, F. Luedtke, V. Dierolf, and K. Buse, "Influence of heat and UV light on the coercive field of lithium niobate crystals," *Appl. Phys. B* **101**, 535–539 (2010).
- <sup>35</sup>M. Schröder, A. Haußmann, A. Thiessen, E. Soergel, T. Woike, and L. M. Eng, "Conducting domain walls in lithium niobate single crystals," *Adv. Funct. Mater.* **22**, 3936–3944 (2012).
- <sup>36</sup>M. C. Wengler, U. Heinemeyer, E. Soergel, and K. Buse, "Ultraviolet light-assisted domain inversion in magnesium-doped lithium niobate crystals," *J. Appl. Phys.* **98**, 064104 (2005).
- <sup>37</sup>Y. Chen, C. Lou, J. Xu, S. Chen, Y. Kong, G. Zhang, and J. Wen, "Domain switching characteristics of the near stoichiometric LiNbO<sub>3</sub> doped with MgO," *J. Appl. Phys.* **94**, 3350–3352 (2003).
- <sup>38</sup>S. Kim, V. Gopalan, K. Kitamura, and Y. Furukawa, "Domain reversal and nonstoichiometry in lithium tantalate," *J. Appl. Phys.* **90**, 2949–2963 (2001).
- <sup>39</sup>V. Gopalan, Q. X. Jia, and T. E. Mitchell, "In situ video observation of 180° domain kinetics in congruent LiNbO<sub>3</sub> crystals," *Appl. Phys. Lett.* **75**, 2482–2484 (1999).
- <sup>40</sup>V. Y. Shur, "Kinetics of ferroelectric domains: Application of general approach to LiNbO<sub>3</sub> and LiTaO<sub>3</sub>," *J. Mater. Sci.* **41**, 199–210 (2006).
- <sup>41</sup>Keithley Instruments, "Model 6517B Electrometer/High-Resistance Meter Specifications—SPEC-6517B—Rev. C," (2020); see [https://download.tek.com/document/SPEC-6517BC\\_Mar\\_2020.pdf](https://download.tek.com/document/SPEC-6517BC_Mar_2020.pdf).
- <sup>42</sup>T. Volk and M. Wöhlecke, *Lithium Niobate: Defects, Photorefractive and Ferroelectric Switching*, Springer Series in Materials Science (Springer, Berlin, 2008).
- <sup>43</sup>H. Lu, Y. Tan, J. P. V. McConville, Z. Ahmadi, B. Wang, M. Conroy, K. Moore, U. Bangert, J. E. Shield, L.-Q. Chen, J. M. Gregg, and A. Gruverman, "Electrical tunability of domain wall conductivity in LiNbO<sub>3</sub> thin films," *Adv. Mater.* **31**, 1902890 (2019).
- <sup>44</sup>L. Tian, A. Vasudevarao, A. N. Morozovska, E. A. Eliseev, S. V. Kalinin, and V. Gopalan, "Nanoscale polarization profile across a 180° ferroelectric domain wall extracted by quantitative piezoelectric force microscopy," *J. Appl. Phys.* **104**, 074110 (2008).
- <sup>45</sup>N. C. Carville, S. M. Neumayer, M. Manzo, M.-A. Baghban, I. N. Ivanov, K. Gallo, and B. J. Rodriguez, "Influence of annealing on the photodeposition of silver on periodically poled lithium niobate," *J. Appl. Phys.* **119**, 054102 (2016).
- <sup>46</sup>S. Sanna and W. G. Schmidt, "LiNbO<sub>3</sub> surfaces from a microscopic perspective," *J. Phys.: Condens. Matter* **29**, 413001 (2017).
- <sup>47</sup>E. A. Eliseev, A. N. Morozovska, S. V. Kalinin, Y. Li, J. Shen, M. D. Glinchuk, L.-Q. Chen, and V. Gopalan, "Surface effect on domain wall width in ferroelectrics," *J. Appl. Phys.* **106**, 084102 (2009).